International Journal of Greenhouse Gas Control 119 (2022) 103742

Contents lists available at ScienceDirect

International Journal of Greenhouse Gas Control

journal homepage: www.elsevier.com/locate/ijggc

Regolith and host rock influences on CO_2 leakage: Active source seismic profiling across the Little Grand Wash fault, Utah

Lee M. Liberty [a,*], Jonathan Yelton [a], Elin Skurtveit [b], Alvar Braathen [c], Ivar Midtkandal [c], James P. Evans [d]

[a] Department of Geosciences, Boise State University, 1910 University Drive, Boise, ID, United States 83725
[b] Norwegian Geotechnical Institute, Oslo, Norway
[c] Department of Geosciences, University of Oslo, Oslo, Norway
[d] Department of Geosciences, Utah State University, Logan, Utah, United States

ARTICLE INFO

Keywords:
Seismic tomography
CO_2 leakage
Fault permeability
Regolith development

ABSTRACT

Understanding carbon dioxide (CO_2) reservoir to surface migration is crucial to successful carbon capture and sequestration approaches; especially fault/reservoir interactions under injection pressure. Through seismic imaging, we explore regolith and shallow stratigraphy across the Little Grand Wash fault. The presence of natural CO_2 seeps, travertine and tufa deposits confirm modern and ancient fault-controlled CO_2 leakage. We consider this an analogue for a long-failed sequestration site. We estimate bulk porosity and fracture density for host rock, regolith, and fault zone from petrophysical relationships. When combined with existing geochemical and geological data, we characterize a 60 m wide damage zone that represents the primary surface delivery channel for CO_2 originating from reservoir depths. Within this damage zone, low seismic velocities suggest sediments have formed through host rock chemical dissolution or mechanical weathering. In contrast, velocities within the adjacent host rock are consistent with low fracture density clastic rocks. We measure anomalously high seismic velocities within the fault zone along one profile that best represents a sealed (cemented/plugged) low permeability, relic flow channel. This suggests that shallow fault zone permeability varies along strike. While regional stress changes may account for decadal- to millennial-scale changes in CO_2 pathways, we speculate that the total fluid pressure has locally reduced the fault's minimum horizontal effective stress; thereby producing both low- and high-permeability fault segments that either block or promote fluid migration. Studying CO_2 migration in this system can inform potential risks to future sequestration projects and guide monitoring efforts.

1. Introduction

Anthropogenic carbon dioxide (CO_2) release into the atmosphere presents a threat to human civilization in the form of climate change (e.g., Rahman et al., 2017). One strategy to reduce atmospheric CO_2 introduced by human activity is through carbon capture and geologic sequestration (CCS) by which CO_2 from power plants, refineries or other industrial sources is compressed, transported, and injected into a subsurface reservoir for long-term storage (Pacala and Socolow, 2004). Assessing reservoir integrity and predicting post-injection CO_2 migration behavior is vital to a robust CCS program.

For sedimentary rocks, advective flow dominates fluid and gas migration through the pore space in rocks. In the presence of an impermeable seal, CO_2 will remain at depth. A major concern of a CCS approach is the potential for CO_2 to migrate from reservoir depths upwards along pre-existing, high permeability, steep faults or other permeable pathways, through the critical zone, and into the atmosphere. The CO_2 that enters the critical zone can lead to pH changes in soils, change organic productivity through CO_2 interchange, mobilize contaminants that influence ecosystems, and lead to diffusion of CO_2 from the soils to the atmosphere (e.g., Maček et al., 2005; Bergfeld et al., 2006; Patil, 2012). CO_2 at the land surface can also lead to asphyxiation in humans and other animals. Permeable flow paths may require decades or longer for CO_2 to migrate from a viable CCS reservoir to shallow depths. Although it is recognized that faults can provide conduits to deliver CO_2 to the atmosphere (e.g., Lewicki and Brantley, 2000; Annunziatellis et al., 2008), the CSS community has not fully assessed how CO_2 stored within high porosity (ϕ) reservoir rocks may interact

* Corresponding author.
E-mail address: lliberty@boisestate.edu (L.M. Liberty).

https://doi.org/10.1016/j.ijggc.2022.103742
Received 8 December 2021; Received in revised form 21 July 2022; Accepted 28 July 2022
Available online 5 August 2022

with the critical zone or migrate back to the atmosphere at these time scales.

A common source of leakage or seal bypass in subsurface reservoirs is flow within or near fault and fracture zones (Gibson et al., 1989). Fault or fracture permeability is dependent on the mechanical properties of the fault and host rock, the reservoir-scale geometry and structure of the fault zone, the nature of the fault-related rocks within the fault zone, and the temporal variations in the geochemical and mechanical processes in the faults. Properties such as fracture aperture, stress field orientation, and fault, host rock, and fluid constituents all can control flow and leakage rates from depth (e.g., Barton et al., 1995; Miocic et al., 2019). Regolith formation and constituents may also influence permeable channels to the surface; and may contribute to the integrity of a CCS reservoir seal.

To assess the shallow portions above a CCS reservoir, we characterize a naturally leaking CO_2 system through seismic profiling. We acquired data that cross strands of the Little Grand Wash fault (LGWF) system, located in east-central Utah (Fig. 1). Here, the fault truncates the Green River anticline, providing a structural trap and conduit for CO_2 to outgas from reservoir depths to the atmosphere (Shipton et al., 2004; Dockrill and Shipton, 2010; Kampman et al., 2014). Using a seismic tomography approach, we identify and characterize the fault's damage zone, estimate soil/rock ϕ and host rock fracture density, and estimate fluid saturation and pore pressure changes along three profiles. We also characterize the stratigraphy and structure to CO_2 reservoir depths of hundreds of meters with two seismic reflection profiles. We compare our seismic results to CO_2 flux values (Han et al., 2013; Jung et al., 2014) to characterize a high permeability channel that promotes the upward flow of CO_2 through elevated pore pressure within the fault's damage zone. From these measurements, we offer an approach to assess site integrity and leakage rates of a CCS site, and speculate on the role that effective pressure may have to open fractures in a shallow damage zone of a fault system. We note that our approach is not new for mapping and characterizing faults and fractures at a range of scales (e.g., Todd and Simmons, 1972; Michael and Eberhart-Phillips, 1991; Gettemy et al., 2004; Clarke and Burbank, 2011), but our imaging approach has not been applied to potential CCS sites or sites where elevated CO_2 soil flux and pore pressures have been directly recorded.

2. Setting

The LGWF is an east-west trending 60 to 75° south-dipping normal fault located near the northern margin of the Paradox Basin near Green River, Utah (Fig. 1; Baker, 1946; Doelling et al., 2015). This basin hosts a series of natural CO_2 reservoirs (Allis et al., 2001). The fault has a ~30 km long arcuate surface expression, and the central span intersects the crest of the Green River anticline (Shipton et al., 2004; Dockrill and Shipton 2010; Doellling et al., 2015). Within the central span, the fault is segmented, and can be divided into a 30–100 m wide zone with two dominant fault strands (Shipton et al., 2004). Additionally, a series of minor faults and relay ramps are mapped. Fault offset is greatest within the central span of the fault near the Green River and Crystal Geyser, with fault throw upwards of 300 m. Our study consists of three profiles along the central region of the LGWF (Fig. 1).

High-quality reservoir sandstones a few hundred meters below surface in the LGWF footwall are juxtaposed against shales, silts and sandstones within the fault's hanging wall (Shipton et al., 2004; Kampman et al., 2014), suggesting a membrane seal across the fault (Dockrill and Shipton 2010). From outcrop studies, the fault has an estimated 0.7-to-3-meter wide core of foliated clay-rich gouge and a one meter wide highly fractured damage zone (Vrolijk et al., 2005; Jung et al., 2014; Dockrill and Shipton, 2010). Some of the exposed sandstones host mainly cataclastic shear-compaction deformation bands in the damage zone, in many cases localizing significant carbonate cement. This suggests that similar bands bound the fault in subsurface reservoirs. In outcrop, Dockrill and Shipton (2010) identified a 20–30 meter wide zone of fractures surrounding the fault core that may be considered part of the fault's damage zone.

The general bedrock lithology within the upper few hundred meters of the study area consists of gentle north-dipping interlayered reservoir-seal systems of the Jurassic to Cretaceous San Rafael and Cedar Mountain groups. Within the northern footwall block, several sealing shales

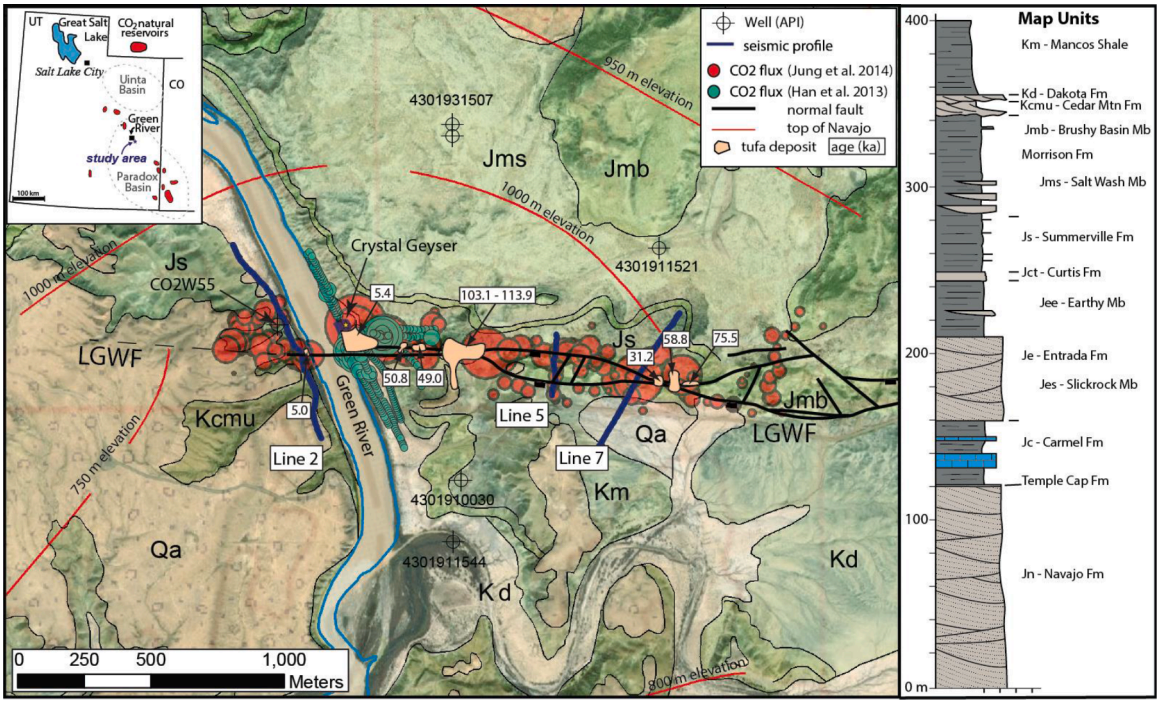

Fig. 1. Aerial image of study area that includes geologic contacts from Doelling et al. (2015), mapped faults and tufa deposits from Burnside et al. (2013), and CO_2 flux measurements from Han et al. (2013) and Jung et al. (2014). Inset map shows the location of the study area within the Paradox Basin in eastern Utah (modified from Han et al., 2013). Well logs were obtained from https://datamining.ogm.utah.gov/.

overlie reservoir sandstones (Fig. 1). In the southern hanging wall block, Cretaceous mudstone-rich Mancos Shale (Km) strata are juxtaposed against thicker footwall sandstones with some localized drag-folding setting up a southward dip that deviates from the gentle northerly dip of the region (Doelling et al., 2015). Between the fault-strands of the LGWF, southerly dips are prominent, suggesting the fault partly accumulated displacement through fault-propagation folding, consistent with a breached monocline geometry captured around the fault zone. Between fault strands, steeply dipping, mostly siltstone and shales of the Brushy Basin member of the Morrison Formation (Jmb) are mapped near our Line 5 and Line 7 (Fig. 1), whereas thin-bedded sandstones and shales of the Summerville Formation (Js) are mapped within the fault zone to the west of the river (Line 2). The 322 m deep CO2W55 borehole, located directly west of the Green River, encountered the Je sandstone from 8.8 to 150 m depth. Located to the north of the main LGWF fault strand but within the faults damage zone, CO2W55 showed CO_2 gas as shallow as 18 m depth (Kampman et al., 2014). CO_2 degassing was intermittent throughout the Je section, where fracture density was highly variable. Fractures were all near vertical and mostly contained to the fine-grained interdune sandstone layers (Skurtveit et al., 2020). One relevant interdune unit is found between 10 and 30 m depth, and is one focus of our Line 2 seismic tomography analysis.

From the surface to the top of Je sandstone near CO2W55 (upper 5–10 m), regolith and Quaternary alluvium from the Green River are mapped (Kampman et al., 2014; Doelling et al., 2015; Fig. 1). These units occupy the top of our Line 2 tomography model. Below the Je section, the Carmel Formation was logged in CO2W55 from 149 m to 200 m depth (Kampman et al., 2014). This low permeability shale, gypsum and siltstone unit acts as a permeability barrier between overlying Je and underlying Navajo sandstones. Within the Carmel Formation, CO2W55 encountered a subsidiary fault strand at 188 m depth, with 76° south dip. The Navajo Sandstone was encountered from 200 to 322 m in CO2W055. From driller's logs, above-hydrostatic-pressure CO_2 gas persisted throughout the Navajo section. On the east riverbank, CO_2-charged eruptions at the Crystal Geyser that were sourced from this reservoir constitute multi-hour eruptions with water temperature consistent with the region's geothermal gradient and a unique microbial community (Baer and Rigby, 1978; Probst et al., 2018).

3. CO_2 leakage

Previous studies have revealed that the central portion of the LGWF acts as a vertical conduit for the upward flow of CO_2-charged fluids (e.g., Baer and Rigby, 1978; Heath et al., 2009; Dockrill and Shipton, 2010; Han et al., 2013; Jung et al., 2014). Hood and Patterson (1984) measured artesian pressures within underlying reservoir rocks (i.e. Navajo sandstone). Coupled with these elevated pressures, Naruk et al. (2019) showed that the addition of a pre-existing vertical fracture network is needed to produce the observed surface seeps and geysers.

Although there is no direct evidence for post-Neogene motion along the LGWF, low magnitude seismicity has been documented. This suggests modest rates of strain accumulation and release for the region (Han et al., 2013). These conditions and observations support the Caine et al. (1996) model for a fault zone and its permeability structure; in the presence of a thin fault core and broad damage zone, a fault likely acts as a high permeability conduit for vertical fluid flow. Additionally, Zoback et al. (1987) suggested that stressed faults require elevated permeabilities within the fault's damage zone when compared to the matrix permeability of the host rock. Thus, reservoir rocks and overlying regolith must consist of lower permeabilities when compared to materials within the fault's damage zone.

Along the LGWF, geysers, springs, and ancient travertine deposits suggest CO_2-charged fluids have leaked to the surface for nearly 500,000 years (Burnside et al., 2013; Fig. 1). Relic travertine deposits as crusts on hilltops reflect progressive exhumation during CO_2 seep events. These travertine layers are distributed along about three km of the fault's proximal footwall, indicating spatial and temporal changes in the primary CO_2 flow pathways. Changes in seepage points may be the result of fracture self-sealing via carbonate vein development, seismicity that alters regional stresses, or local changes in aquifer conditions (e.g., Han et al., 2013). Jung et al. (2014) found that these relic pathways still record elevated CO_2 soil flux values, suggesting that absolute self-sealing of ancient fluid pathways may be difficult.

The Crystal Geyser, located in the central portion of the LGWF (Fig. 1), erupts at intervals that match four distinct cycles (e.g., Han et al., 2013). The geyser contains the shallow portion of the drill stem from an 800 m deep hydrocarbon exploratory drill-hole, Ruby X-1, drilled in 1935. Water chemistry, temperature, microbial communities, and pressure studies from these eruptions provide clear evidence for three or more reservoirs that recharge and release CO_2 (Baer and Rigby, 1978; Heath et al., 2009; Han et al., 2013; Probst et al., 2018). These studies note that the more prolonged multi-hour eruptions are sourced from the Navajo Sandstone at 200 to 300 m depth. Detailed logs and chemistry from the Ruby X-1 well are not available due to the drilling age and abandonment of the well from overpressured conditions.

4. Physical property relationships

Seismic velocities directly relate to a material's elastic moduli and bulk density. For soils, regolith and bedrock, influences on seismic velocity include ϕ, pressure, lithology, grain shape, and the fluid or gas that occupies the pore space (Mavko et al., 2020). In our study area, we placed seismic profiles on mobilized soils (fluvial and alluvial deposits) that directly overlie regolith on portions of two of our profiles (Line 2 and Line 7) and upon exposed regolith and rock along portions of Line 5 and Line 7 (Fig. 1).

To assess the upward flow of CO_2 under natural or CCS conditions, the matrix ϕ and fracture density of the host rock and overlying regolith must be estimated. Higher matrix ϕ rock tends to have more interconnected pore space and therefore higher permeability. Both empirical datasets and rock physics models suggest a direct relationship between seismic velocity and ϕ for clastic rocks (e.g., Castagna et al., 1985; Mavko et al., 2020). Furthermore, there is generally a direct relationship between ϕ and permeability (e.g., Ehrenberg and Nadeau, 2005). Thus, seismic velocity mapping is a viable approach to assessing permeable pathways within sedimentary rocks.

Although it is difficult to differentiate lithology with seismic velocity measurements alone, shales and mudstones that dominate the shallow hanging wall (Mancos Shale) generally contain more clay than the mainly sandstone and subordinate shales that occupy the footwall. Increased clay content generally reduces both p-wave (V_p) and shear wave (V_s) velocities (Mavko et al., 2020). Jung et al. (2015) compiled ϕ and permeability values for the study area, and estimated the reservoir sandstones within the footwall block contain ϕ between 20 and 30%, compared to ϕ for the hanging wall shales that range from 10 to 20%. Their compilation, and a previous study (Hood and Patterson, 1984) suggested two-orders of magnitude higher permeability for the footwall sandstone units when compared to the hanging wall shale-rich formations. Presumably, these permeability relationships extend into the regolith, or critical zone, where weathered bedrock materials are preserved.

Porosity distribution, water storage potential, and regolith formation above unweathered bedrock is an important aspect to CCS site assessment. Unconsolidated sediments from deposition or erosion often contain bulk ϕ greater than 30% (e.g., Marion et al., 1992; Holbrook et al., 2014; Zimmer et al., 2007; Flinchum et al., 2018; Uyanik, 2019). For the LGWF region, the high permeability regolith sands show elevated CO_2 and CO_2 soil flux values that suggest high advection rates through the regolith above the footwall and within the LGWF (Jung et al., 2014). Low CO_2-enriched soils above hanging wall rocks suggest low permeability and low diffusion rates to the south of LGWF.

Although gas can influence seismic velocity, CO_2 saturation has little

effect on Vp within unsaturated materials. This results from the density and Vp of CO_2 being similar to that of air at surface pressures and temperatures. Results of laboratory experiments on saturated sandstone samples indicate a ~5% Vp reduction at 25% or higher CO_2 concentration (Gutierrez et al., 2012). Numerical simulations by Yamabe et al. (2016) predict a 9% Vp decrease at full saturation of CO_2 (equilibrium state). Given that our model uncertainties, we neglect the direct influence of CO_2 on seismic velocity and focus our interpretations only on fluid, soil, and rock bulk properties from our velocity tomograms.

For our study, we generalize rock properties and assign velocity bounds. We estimate these bounds for unsaturated soil or regolith, saturated soil or regolith, fractured or high ϕ dry rock, fractured or high ϕ saturated rock, and unfractured, low ϕ rock (Table 1). These velocity bounds are aligned with rock physics models and empirical soil and rock relationships (e.g., Marion et al., 1992; Lee, 2003; Prasad et al., 2004; Holbrook et al., 2014; Zimmer et al., 2007; Mavko et al., 2020). Additionally, we utilize direct laboratory measurements from a range of dry sandstones samples, with varying silt and clay content, found in our study area.

5. Porosity estimates

Vp is strongly controlled by the material that occupies the pore space (Nur et al., 1998; Mavko et al., 2020). In the presence of full saturation, Vp generally increases beyond the fluid Vp, or greater than about 1500 m/s. In contrast, Vs of sediments is more controlled by matrix properties. For example, using standard soil classifications, Vs=360 m/s separates soft from stiff soils; Vs=760 m/s separates stiff soils from rock; and Vs>1500 m/s represents unaltered bedrock (Building Seismic Safety Council (BSSC) 2009).

To estimate ϕ from Vp (m/s) for saturated bedrock, we adopt the Castagna et al. (1985) empirical relationships from the Frio Sandstone:

$$V_p = 5810 - 9420 * \phi - 2210 * V_{cl} \quad (1)$$

where V_{cl} represents percent formation clay content. As shown in (Brocher, 2005), this equation provides a reasonable and global fit to many saturated clastic rocks, and extends from consolidated to unconsolidated materials. For our analysis, we use V_{cl} =20%, consistent with Je that lies immediately below the elevation of the Green River within the LGWF footwall block of Line 2 (Dockrill and Shipton, 2010). We also use these relationships for Line 7, where artesian springs saturate surface soils.

Unaltered Je sandstone (Aeolian dune) shows of about 25% ϕ at reservoir depths (Ridgley and Hatch, 2013), but ϕ may be lower for more clay-rich sedimentary facies. Antonellini and Aydin (1994) measured ϕ in the Moab member of Je to vary from 4 to 28%. Other reservoir sandstones in the study area show similar ϕ ranges (Hood and Patterson, 1984). Thus, we anticipate Vp for unaltered sandstones to exceed 3000 m/s (equation 1; table 1). We compare this value to the portion of our models that lie below regolith and outside the damage zone of the LGWF. Although we acknowledge that absolute ϕ requires direct sample measurements, we rely on our ϕ estimates to identify relative changes that may point to higher permeability CO_2/fluid pathways when compared to unaltered bedrock. We note that the velocities will be reduced in the presence of increasing clay content, as may be expected within the fault's core and with other lithologies that have been regionally mapped (Dockrill and Shipton, 2010; Doelling et al., 2015).

From laboratory measurements, we obtain a direct relationship between dry sandstones at low confining pressures for a range of sedimentary facies in the Je sandstone in our study area (Skurtveit et al., 2021). Vp is measured in unconfined compressional strength tests on dry samples and porosity for each plug calculated from the plug bulk density and particle density (Table 2). An average velocity to porosity relation is calculated for 2.0 MPa stress conditions and a depth dependency is derived based on the variation in velocity measurements at stress below 2.5 MPa. Combined this provides a relationship for Vp including stress and porosity:

$$V_p = (107 * \sigma_1) - (43 * \phi) + 2770 \quad (2)$$

where σ_1 is the vertical stress in MPa. We apply this relationship to the dry sandstones inferred at shallow depths along Line 5.

6. Fault zone or fracture characteristics

Host rock can be damaged through accumulation and release of strain through faulting. Faults constitute a tabular zone of core surrounded by broad damage zone that, in many cases, extend to the earth's surface. Structural elements in faults, such as fractures, deformation bands, fault rocks and rock lenses, and their intrinsic distribution, can either increase or decrease permeability. For instance, within the damage zone, significant fracturing can cause a relatively low ϕ host rock to transform to high ϕ rock volume. For the LGWF, the thin fault core with high shale content is bound by the wide damage zone, as documented from outcrop and CO_2 flux surveys (Dockrill and Shipton, 2010; Han et al., 2013; Jung et al., 2014).

The conditions needed for a fault to behave as a conduit for CO_2 surface outgassing include: 1) an initial pressure gradient to drive upward CO_2 flow; 2) the pore fluid pressure must reduce the effective stress to approximately zero (Zoback et al., 1987; Naruk et al., 2019); and 3) there must be pre-existing high ϕ fractures within the fault's damage

Table 1
General lithology, seismic velocity and porosity (ϕ) ranges. Adapted from Lee (2003).

Lithology	Vp (m/s)	Vs (m/s)	Vp/Vs	ϕ (%)
dry regolith sediment	<1500	<760	<2.5	>30
saturated regolith sediment	1500–2500	<760	>5	>30
semi-consolidated or fractured (dry)	1500–2500	760–1000	<2.5	25–30
semi-consolidated or fractured rock (saturated)	2500–3000	760–1000	>2.5	25–30
unfractured rock	>3000	>1500	<2.5	<25

Table 2
Overview of P-wave velocity (Vp) and porosity measured on dry Entrada Sandstone (Je) plugs from four units in Humbug Flats (Skurtveit et al., 2021).

Unit	Entrada Sandstone Facies	Grain size	Vp at 2 MPa [m/s]	Dry Density [g/cc]	Porosity [%]
L3	Costal dunes	Fine to medium	1663	1.94	26.8
L4	Interdune and sabkha	Clay to very fine	1820	2.28	14.0
			1846	2.25	15.1
			1855	2.26	14.7
L6	Aeolian dunes	Very fine to fine	2535	2.42	8.7
			2486	2.42	8.7
			2483	2.43	8.3
			2468	2.44	7.9
			2485	2.44	7.9
			2437	2.44	7.9
			2107	2.18	17.7
			2143	2.19	17.4
			2047	2.17	18.1
			2131	2.19	17.4
			2251	2.22	16.2
L7	Aeolian dunes	Very fine to fine	2192	2.33	12.1
			2119	2.30	13.2
			2193	2.31	12.8
			2044	2.31	12.8
			2328	2.34	11.7
			2282	2.34	11.7

zone. In other words, mineral precipitation or cementation within the fault zone, and diffusive flow through the soils, is negligible. Effective stress, or effective pressure, on a fault system can directly influence seismic velocity. A fault system under high effective pressure will likely act as a barrier to upward fluid or CO_2 migration. Conversely, increasing pore fluid pressure within a fault zone can open pre-existing fractures and reduce the effective stress. A combination of high pore pressure and low effective pressure within the fault's damage zone can increase soft porosity (i.e., the aspect of ϕ that changes with pressure), thereby increasing fracture-related ϕ, reducing grain-to-grain contact, and decreasing seismic velocity. High pore pressure persisting over long periods of time can inhibit diagenesis (e.g., cementation within a fault), preserve high ϕ conditions, and keep seismic velocities low (Mavko et al., 2020). These open pathways that often form at high angles to the earth's surface, can promote upward fluid or CO_2 migration.

Clarke and Burbank (2011) developed an equation to estimate fracture density (P_f) from the measured velocity (V), the velocity derived from unaltered rock (V_r), and the velocity of the fracture filling material (V_f).

$$P_f = \frac{V_f}{(V_r - V_f)} * \left(\frac{V_r}{V} - 1\right) \quad (3)$$

They applied this relationship to shallow bedrock using first arrival velocity estimates. Assumptions to satisfy this relationship include a single material filling the void space (e.g., water or air) within bedrock; that the seismic rays propagate laterally through the fractures (e.g., vertical fractures and horizontally traveling seismic ray paths); and that the state of stress is not a controlling factor in the shallow subsurface. For our study, we assume that V_r is best represented by the maximum velocity in each tomogram. The assumption of horizontal ray paths and vertical fractures is valid for materials below the near surface and for the steep faults mapped in the study area. (e.g., Dockrill and Shipton, 2010). To focus on horizontal ray path coverage, we exclude the depths where soil or regolith is inferred (<2000 m/s), as these slower velocities bend returning raypaths toward the surface. For our profiles where we interpret fully saturated rock at shallow depths, we derive P_f from our Vp tomograms assuming the pore space is filled with water or high porosity sediments; $V_f = 1500$ m/s. Where dry rock conditions are presumed, we use $V_f = 900$ m/s as the Vp for unsaturated near surface sediments (e.g., Lee, 2005; this study). To estimate P_f from Vs tomogram, we assume Vs=500 m/s for soils occupy the pore space. We acknowledge that our assumptions are an oversimplification for this field site, but we use this analysis to identify relative changes in fracture density across each profile. To emphasize these lateral fracture density changes, we also vertically average our measurements to highlight broad, highly fractured zones.

7. Seismic approach

We present results from three north-south seismic profiles acquired in 2019 and 2020 (Fig. 1). Additional profile results are summarized in Yelton (2021). Each line crosses the LGWF near the center of the geophone spread. Two profiles cross high CO_2 flux regions within the LGWF and one profile crosses the LGWF where low CO_2 flux measured were documented (Jung et al., 2014). The latter profile crosses a former, assumed plugged (cemented or mineralized) CO_2 conduit. We present three Vp tomographic profiles obtained from vertically polarized first arrivals, one Vs tomogram from horizontally polarized first arrivals, and two Vp reflection profiles.

Seismic shot gathers show clear first arrivals for most source-receiver offsets, and reflectivity before the slower surface waves (Fig. 2). We pre-processed the seismic field records by assigning source-receiver geometries from differentially corrected GPS positions, removing bad traces, and bandpass filtering. We stacked common source-receiver traces to improve signal quality. We picked coherent first motions that contained a center frequency of about 50 to 70 Hz.

7.1. First arrival tomography

For our tomograms, we follow the approach of (Clair, 2015) to obtain velocity models from first arrival picks. We start our inversion with a one-dimensional velocity model draped from the surface topography. We calculate the difference between our modeled picks and calculated arrival times of the initial model obtained from shortest path ray tracing (Moser, 1991). The calculated misfit is then mapped to a model update through a linear inversion. The raytracing-inversion process is repeated until the root mean square (RMS) misfit is similar to our estimated data uncertainty; less than about three milliseconds (ms). The inverse problem is stabilized with first and/or second order derivative operators (Tikhonov regularization). Because we expect sharp lateral boundaries on the edges of the fault zone, we use the L1 norm to minimize model roughness. At each inversion step, our approach finds a smooth model update, then reweights the smoothness constraint. Thus, regions where the data support a sharp boundary receive a smaller roughness penalty. The inversion is repeated until we obtain a stable global smoothness norm.

Because we recognize that our first arrival tomographic modeling approach produces non-unique solutions, we utilize shot and common offset gathers (COG) to validate our first-order observations (Fig. 2). By looking directly at the waveforms, we address any picking bias incorporated into our inversion models. We assume that arrival times will follow a smooth path for a 1-D velocity model (e.g., Schuster et al., 2017; Liberty et al., 2021). First arrivals that show lagging travel times across multiple traces support a low velocity zone (LVZ) near the receiver locations. Conversely, faster first arrivals across multiple traces support the presence of a high velocity zone (HVZ). For our Line 5 shot gather, we note a ~30 m wide HVZ centered near position 145 m.

We show the Line 2 100-m offset COG with a spiking deconvolution operator and 20 to 120 Hz passband filter applied (Fig. 2). Deconvolution attenuates wave path multiples and sharpens the seismic pulse (Yilmaz et al., 2001). We note slower first arrivals between positions 480 m and 540 m, consistent with a broad LVZ. These surface locations coincide with the mapped fault trace of Doelling et al. (2015).

We also include a 3–15 Hz passband filter for the 50-m offset Line 2 COG that emphasizes surface wave arrivals for each source-receiver midpoint location (Fig. 2). Surface waves at these frequencies are most influenced by Vs distributions within the upper 10′s of meters, consistent with our tomographic model depths. Again, a COG for a 1-D velocity model would produce near constant arrival times, and lateral travel time changes in surface waves suggest lateral velocity changes. We note a travel time lag in the same ~60 m wide zone that supports a LVZ centered near position 510 m. Additionally, we include two dispersion images that highlight fundamental Rayleigh wave speeds. The two dispersion plots were derived from shot/receiver pairs that lie on either the hanging wall or footwall side of the LGWF. These plots highlight a ~1400 m/s Rayleigh wave speed average to the north of the fault and a ~1000 m/s Rayleigh wave speed average to the south of the LGWF. This velocity change is consistent with changing lithology across the LGWF (Fig. 1).

7.2. Seismic reflection

We processed seismic reflection profiles using Halliburton's SeisSpace® processing software with a standard processing approach outlined by (Yilmaz et al., 2001). Processing steps include datum statics, spiking deconvolution, bandpass filter, surface wave attenuation through a two-step singular value decomposition approach to estimate and adaptively subtract the ground roll signal (where appropriate), iterative velocity analyses with dip moveout corrections, amplitude gains, and a post-stack time to depth conversion. Where surface waves were strong, this window was muted. Post-stack migration is selectively

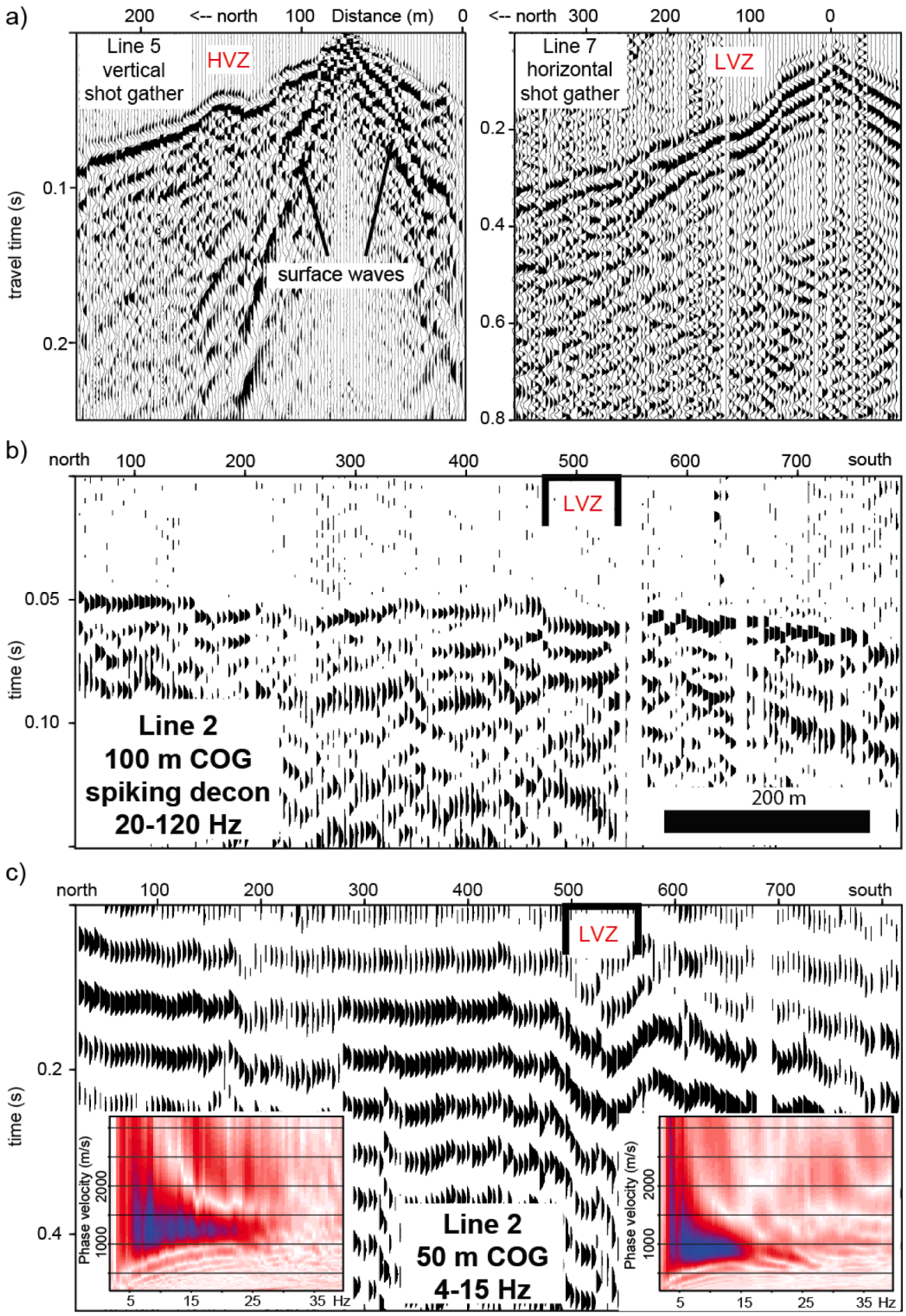

Fig. 2. a) Vertical shot gather from Line 5 and horizontal (shear) shot gather from Line 7 showing clean first arrivals. Fast arrivals support a HVZ and delayed arrivals support a LVZ, both zones within the LGWF; b) Line 2 COG (100 m source-receiver offset) with a spiking deconvolution and 20–200 Hz passband filter to emphasize first arrivals and a LVZ at the LGWF; c) Line 2 COG (50 m source-receiver offset) with a 4–15 Hz passband to emphasize surface wave energy. Surface wave dispersion images from hanging wall and footwall sides are also shown to emphasize changing velocities across the LGWF.

applied to the data where appropriate so as to not introduce migration artifacts which can distort key reflector geometries. Depths were estimated using 1-D averaged stacking velocity models. These velocities are consistent with previous seismic studies from central Utah (e.g., Stockton and Balch, 1978).

8. Results

8.1. Line 2

The Line 2 profile was acquired using a 35-kg accelerated weight drop source between each of 168–10 Hz 5-m spaced vertical geophones. This 840 m long profile was located along the west bank of the Green

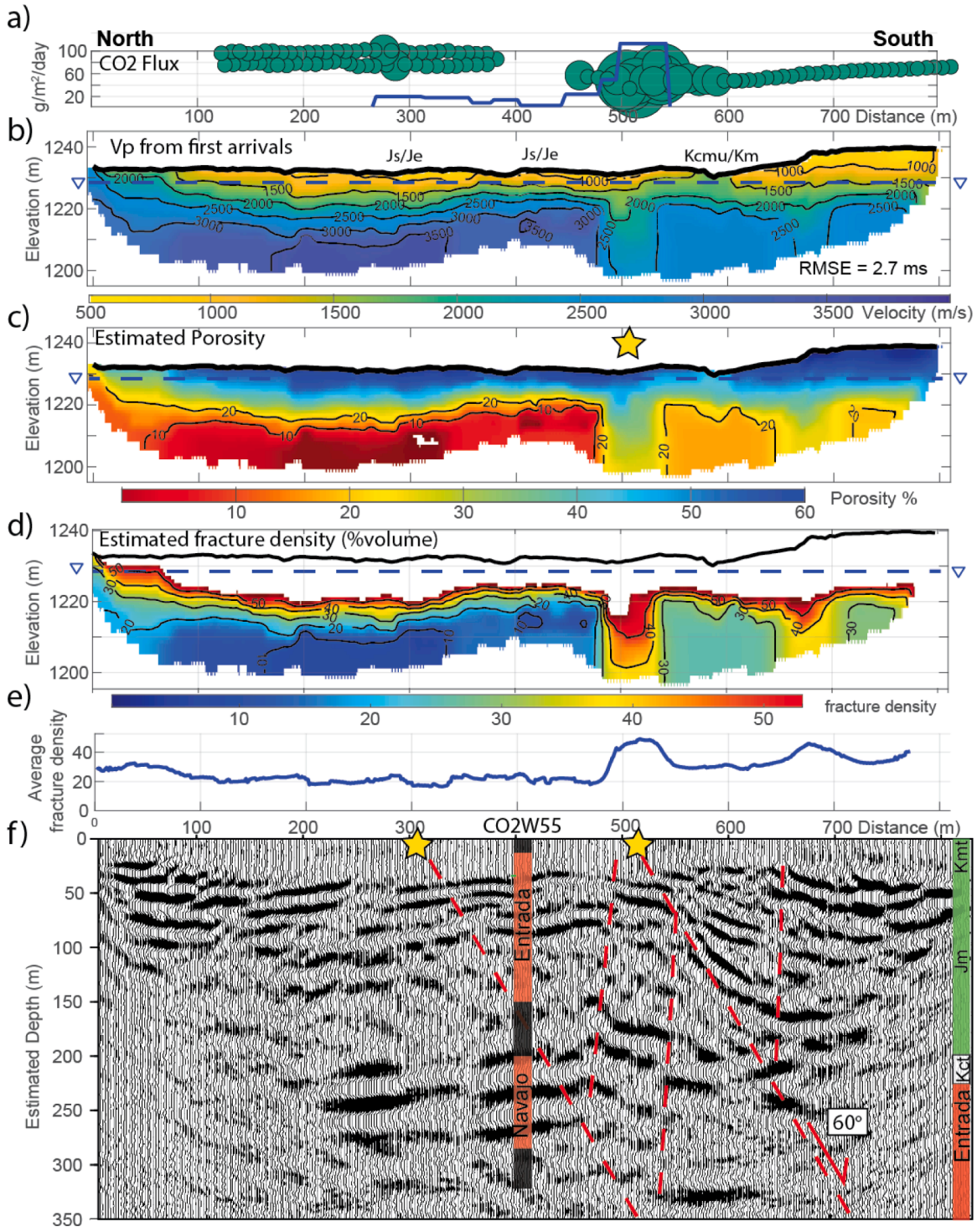

Fig. 3.. a) Line 2 interpolated CO2 flux measurements of Jung et al. (2014) (blue line) and Han et al. (2013) (green circles). Circle size represents a relative CO2 flux magnitude where background flux values represent the smallest circle size; b) Vp tomogram with lithology (Doelling et al., 2015; Kampman et al., 2014). Note that while Js is mapped at the surface, Je is observed beneath the soils in CO2W55; c) Porosity estimate using Eq. (1); (d) Fracture density estimate for Vp>2000 m/s using Eq. (3). Blue dashed line represents the Green River elevation; (e) Vertically averaged fracture density from (d). f) Reflection profile with interpretation. Borehole interpretations are from Kampman et al. (2014). Star represents tufa deposits.

River (Fig. 1), with a surface elevation that ranges from 1234 to 1240 m (Fig. 3). Here, a thin layer of overbank sediments lie above Je sandstones (Kampman et al., 2014; Skurtveit et al., 2020). The CO2W55 borehole was located approximately 50 m west the 400 m distance marker of the profile. This borehole was located about 90 m to the north of the main LGWF trace (position 490 m) and a south-dipping fault identified in CO2W55 projects to the surface near 300 m distance. CO_2 flux measurements ranged from 2.4 to 111.3 g/m^2/day between about 260 to 550 m distance (Jung et al., 2014; Fig. 3). The highest CO_2 flux values were recorded between 500 and 550 m distance, adjacent to travertine dated at 5029 +/- 31 years, and where Burnside et al. (2013) mapped the LWGF (Fig. 1). Within the travertine, CO_2-charged bubbles surfaced along the Green River shoreline. CO_2-charged zones within the Je and Navajo sandstones, identified in borehole CO2W055, suggested a permeable pathway between sandstone reservoirs and a broad zone surrounding the LGWF. CO_2 fluxes were not measured along the northern or southern portions of Line 2, but a profile along the eastern bank of the Green River revealed background CO_2 flux values of less than 1 g/m^2/day to the north and south of the identified fault strands (Han et al., 2013; Figs. 1 and 3);

Due to overhead powerlines, the southern 40 m of this profile did not produce clean first arrivals. From arrivals picked at all other source and receiver locations, we produce an 800 m long tomogram with an RMS error of 2.7 ms. Ray coverage extends to about 30 m depth (Fig. 3). Vp ranges from about 800 to 3600 m/s. The depth to the 1500 m/s contour along most of the profile is close to the measured Green River elevation of 1228.5 m, consistent with water saturated sediments or rock below river level (Table 1). The depth to the 2500 m/s contour is about 10 m depth near the CO2W055 borehole, consistent with a regolith base identified at 10.2 m depth (Kampman et al., 2014). These two velocity contours and observations support our velocity/lithology relationships (Table 1).

Near 500 m distance, we note the presence of a 60 m wide, slow, low-vertical gradient Vp zone that we relate to the LGWF damage zone (Fig. 3). This LVZ coincides with a broad zone of elevated CO_2 flux values measured on both the east and west riverbanks (Han et al., 2013; Jung et al., 2014), and was observed on field shot and COG records (Fig. 2). Farther south, and within the hanging wall, Vp is slower than the region to the north of the LGWF. We attribute the slower hanging wall Vp to the presence of clay-rich lithology of the Km or Cedar Mountain (Kcmu) shales (Doelling et al., 2015; Fig. 1). Validating our model, we note slower Rayleigh wave speeds within the LVZ region compared to either the ~1400 m/s Rayleigh wave speeds to the south of the LGWF and the ~1100 m/s Rayleigh wave speeds identified to the north of the fault (Fig. 2). We identify second slow Vp zone beneath the regolith between 650 and 710 m distance, but this slow zone does not extend into the upper 10 m of our tomogram.

Below the 2500 m/s contour, between 0 and 340 m distance, we estimate a bulk ϕ upwards of 30%, with the highest Vp/lowest ϕ at 305 m distance (Fig. 3). Between positions 340 m and 480 m distance, and beneath the regolith, Vp decreases, thus estimates of bulk ϕ slightly increase between two strands of the LGWF (Eq. (1)). For example, at the location of drill hole CO2W55, we estimate 7% ϕ at about 20 m depth. This is similar to the 6% matrix ϕ measured from core sample at 25 m depth (Skurtveit et al., 2020). Shallow sediments, above river level, show ϕ values upwards of 60%. While this appears anomalously high, we note Uyanik (2019) estimated similar ϕ values for clay-rich alluvium from both laboratory and field-based seismic measurements.

Assuming V_r=3600 m/s (fastest measured velocity at 305 m distance) represents unfractured Je sandstone, and V_f=1500 m/s represents the fluid filling the pore space, we estimate fracture density for Line 2 (Eq. (3)). We perform this analysis beneath the 2000 m/s contour to eliminate fracture density estimates within the regolith (Fig. 3). We estimate about 50% fracture density for the top of our model, decreasing with depth. We acknowledge that the estimates near the top of our model may be driven by the presence of some weathered materials or improper assumptions in Eq. (3), and may not reflect host rock properties. Near the bottom of our model, we estimate a fracture density between 0 and 15% between 0 and 300 m distance and fracture density increases to about 20% between the strands of the LGWF. Within this region, one to three vertical fractures per meter were noted within the fine-grained interdune layers identified in well CO2W55 (Skurtveit et al., 2020).

Within the broad LVZ centered near position 510 m, we measure a fracture density above 40%, but this damage zone may be better represented as regolith rather than fractured rock. We note that our fracture density estimates to the north of the low velocity damage zone are poorly appraised due to the changing lithology and our estimate of a constant Vp for unfractured host rock. To obtain a more accurate fracture density estimate for hanging wall rocks, we would need to estimate V_r for unfractured Km rocks. Regardless, we estimate a fracture density change of about 30% within the 60-m wide LGWF damage zone when compared to regions within the footwall block; and we measure moderately higher fracture density between the two mapped strands of the LGWF when compared to the region to the north.

We relate the stratigraphy identified within the CO2W55 borehole to our seismic reflection results (Fig. 3). Our image shows coherent reflectivity within both the Je and Navajo sandstone reservoirs to the north of the LGWF. The upper portion of Je shows more coherent reflectivity compared to the bottom half, perhaps related to siltstone layers that lie between sandstone units in the upper 100 m (Kampman et al., 2014). The Carmel Formation lies beneath the Je sandstones. This unit does not show coherent reflectivity, perhaps related to the fine gypsum, siltstone and sandstone layers that are thinner than our seismic resolution. We identify reflectors near the inferred top and bottom boundaries of the Navajo Sandstone that represent lithologic changes that bound this massive sandstone unit.

To the north of the LGWF, reflectors gently dip to the north. We note that this dip may explain the higher fracture density that we measure between 340 and 480 m distance, as we may simply be measuring updip lithologies that contain fewer natural fractures. Near 420 m distance, offset reflectors change dip direction, consistent with a broadly faulted, asymmetric anticline. We note that reflector truncations best match north- and south-dipping faults, with the fault zone extending for more than 300 m distance. Steeper dips appear to the south of 500 m distance, consistent with a transition in stratigraphy across the LGWF from a 60° south-dipping normal fault. Reflector offsets near the northern LGWF strand, as defined by surface outcrop and borehole logs (Kampman et al., 2014; Skurtveit et al., 2020), show little measurable offset. This is consistent with a low-permeability fault; as lower CO_2 soil flux values were reported here when compared to the southern fault. Other reflector discontinuities are consistent with small offset faults or fracture zones. We map two steep north-dipping faults between the two south-dipping faults. These two faults surface near the main LGWF surface expression and may help deliver CO_2 from reservoir depths.

From our tomogram, rock physics relationships, and reflection image, we interpret Line 2 to consist of unsaturated sediments above the elevation of the Green River and saturated unconsolidated regolith to about 10 m depth along much of the profile (Fig. 3). We interpret semi-consolidated or fractured Je sandstones below the regolith and the most competent sandstone beneath northern 300 m of the profile. The reflection profile supports two ~60° south-dipping faults. The southern fault represents the main strand of the LGWF. Aided by downhole lithologic logs, we observe about 220 m of displacement from the top of the Je unit across the fault zone (Shipton et al., 2004; Kampman et al., 2014; Naruk et al., 2019). The 60-m wide LVZ represents saturated regolith within the broad high ϕ damage zone, consistent with a high permeability fault that delivers CO_2 from reservoir depths to the ground surface and atmosphere. Between the mapped strands of the LGWF, we identify a faulted region that contains slower bedrock Vp compared to similar depths to the north, consistent with a broad, elevated permeability fracture zone that supports CO_2 soil flux values above

background levels. We interpret an additional fault centered at 690 m, but this region shows background CO_2 flux values on the adjacent shoreline and does not appear to extend to the land surface. This suggests that there is no permeable pathway to deliver CO_2 to the surface within this presumed fault strand. Here, low CO_2 flux could be related to a lower permeability fault or lower permeability host rock or regolith.

8.2. Line 5

We acquired the 240 m long Line 5 profile using 120 two-meter spaced 10 Hz vertical geophones and a 4.5 kg sledge hammer source. Four hammer shot gathers were collected at each shot point located at the midpoints between geophones. The Line 5 profile lies 30 to 50 m above the elevation of the Green River, and approximately 700 m to the east of the Crystal Geyser (Fig. 1). Two strands of the LGWF were mapped near positions 55 and 140 m distance (Burnside et al., 2013). Relatively low CO_2 flux values of 0.7 to 11.2 g/m^2/day were measured along most of the profile, with background values measured near the profile ends (Jung et al., 2014; Fig. 1 and 4). There is some alluvium noted along the surface of this profile, but mostly geophones were placed directly in regolith. Js is mapped to the north of 100 m distance, Jmb is mapped between the two fault strands, and Mancos Shale (Km) is mapped to the south of 150 m distance (Fig. 1; Burnside et al., 2013). Due to the limited profile length and acquisition design, we present only

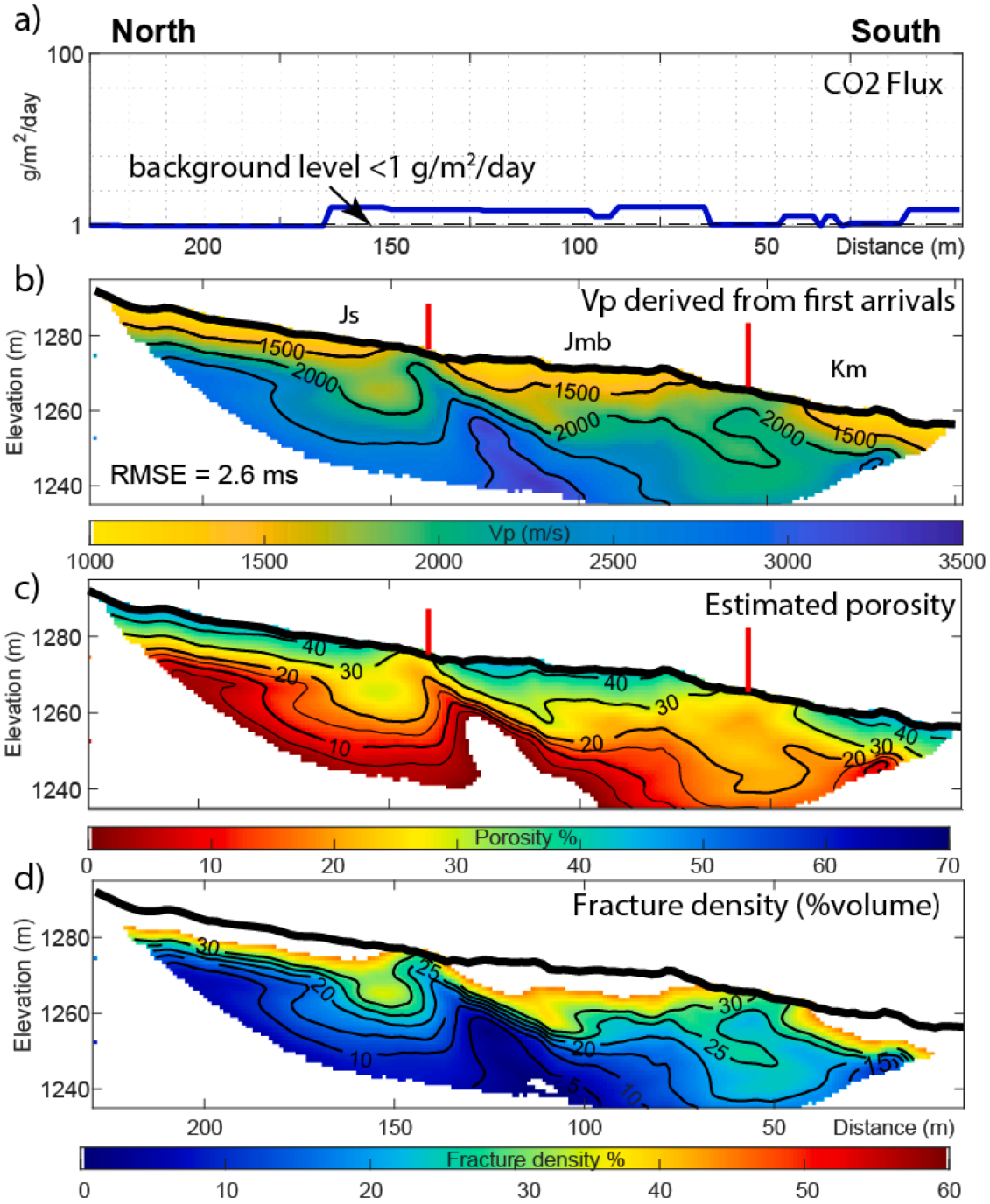

Fig. 4. a) Line 5 interpolated CO_2 flux measurements of Jung et al. (2014), shown as a log-linear plot. Background measurements are estimated at less than 1 g/m^2/day; b) Vp tomogram showing locations of two LGWF strands (red lines) and mapped lithology (Burnside et al., 2013); c) Porosity estimate from laboratory measurements (Eq. (2)); d) Fracture density estimate for Vp>1500 m/s, assuming dry sediments occupy the pore space.

a Vp profile for Line 5.

Our Line 5 tomogram, with an RMS error of 2.6 ms, shows Vp that ranges from 1300 to 3300 m/s (Fig. 4). Given that rock outcrops along this profile, and with an assumption that the depth to groundwater is close to the elevation of the Green River, we interpret hanging wall rocks that lie in the upper 30 m beneath Line 5 as dry, fractured or semi-consolidated rock. Unlike Line 2, we see no broad, low Vp zone associated with the main strand of the LGWF. Instead, between 110 and 140 m

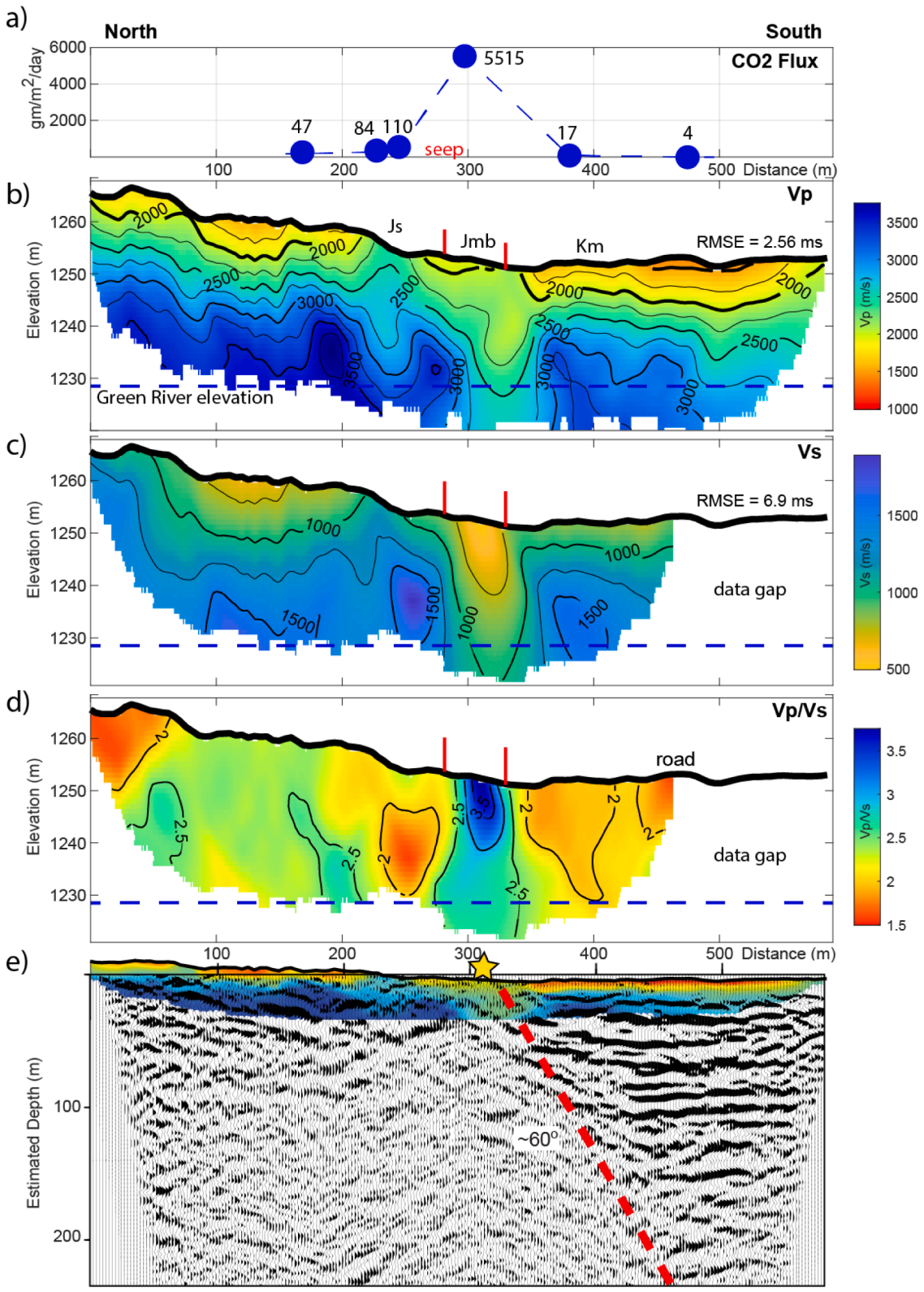

Fig. 5. a) Line 7 CO_2 flux measurements of Jung et al. (2014); b) Vp tomogram showing locations of two LGWF strands (red lines; Burnside et al., 2013) and lithology (Doelling et al., 2015); c) Vs tomogram showing locations of two LGWF strands; (d) Vp/Vs profile from (b) and (c); (e) Reflection profile with interpretation. Blue dashed line represents the Green River elevation. Yellow star represents the location of CO2 seeps observed during field work.

distance, we observe a ~60° south-dipping, anomalously high Vp zone. This 30-m wide HVZ zone is observed on the field records (Fig. 2) and is consistent with either lower ϕ dry rock or fully saturated stiffer rock within the LGWF (Table 1). If this zone represents a high permeability saturated zone, we would have expected higher CO_2 flux values than what was measured (Jung et al., 2014), as advective flow dominates the CO_2 outgassing signal through elevated fluid and pore pressures. Instead, we interpret the HVZ to a sealed fault and relic flow pathway. We identify a second, more modestly elevated HVZ centered near position 60 m. This is close to another mapped LGWF strand (Burnside et al., 2013; Fig. 1), but the geometry of the presumed fault is unclear from our tomogram.

We estimate ϕ from Vp using our dry sandstone laboratory measurements (Table 2; Eq. (2)). We note ϕ <30% for most of the profile, attributed to rock that outcrops along the length of Line 5. We estimate ϕ <10% for the base of our model, consistent with our footwall ϕ of Line 2, shallow ϕ borehole estimates from CO2W55, and a low ϕ sandstone lithology. Within the south dipping high Vp zone, ϕ approaches 0%. We attribute this to either fully cemented sandstone or to a stiffer lithology within the fault core and damage zone compared to our laboratory samples (Table 2). Our fracture density estimate, assuming dry sediments occupy the fracture space ($V_f = 900$ m/s), is consistent with a low fracture density sealed fault. We note slightly lower estimates of ϕ and slightly higher fracture density estimates along the southern portion of Line 5 that we attribute to a lithologic change to the more shale-rich Km unit.

In summary, we observe little regolith or soil layer above dry rock on our Line 5 tomogram. We interpret the dominant feature on this profile as a high velocity/low ϕ relic south-dipping fault that has limited upward flow of CO_2 or fluid. CO_2 flux values near background levels, coupled with our seismic observations, suggest a cemented and sealed fault with little evidence for diffusive flow to the surface. The HVZ width matches fault zone width estimates in outcrop (Dockrill and Shipton, 2010).

8.3. Line 7

Line 7, located along a broad drainage, lies approximately 1000 m to the east of the Crystal Geyser and Green River (Fig. 1). The profile elevation ranges from 1251 to 1267 m, between 18 and 34 m above the Green River elevation (Fig. 5). The profile crosses two closely spaced south dipping fault strands of the LGWF at a distance of 280 m to 330 m along the profile (Burnside et al., 2013). Between about 280 to 300 m distance, Jung et al. (2014) mapped an area where elevated CO_2 soil flux was measured at 5514.7 g/m^2/day (Fig. 5). This measurement was the highest natural CO_2 source measured for the region, only slightly less than that measured at the Crystal Geyser borehole. Between 250 to 300 m distance, water and gas bubbles appear from an artesian spring. On the northern footwall block, Doelling et al. (2015) mapped thin-bedded Js sandstone-shale sections, likely extending to the bottom of our tomography model. Within the southern hanging wall block, Quaternary alluvium was mapped above Km. Jmb is mapped between 280 and 320 m distance, between two mapped fault strands of the LGWF.

Our Vp dataset consists of 120 5-m spaced 10 Hz geophones, with shots acquired between each geophone. We used a 4.5 kg sledge hammer source with four to nine shots per source location. We also acquired a Vs profile using both east- and west-directed horizontal sledge hammer hits and 96 10-Hz five-meter spaced horizontally polarized geophones. At each shot location, four horizontal shots were recorded with source motion initiating eastward, then four shots were recorded with source motion initiated westward at the same shot location (Fig. 2). We did not acquire Vs data across the southern 120 m of the Vp profile.

Vp/Vs is considered as a primary indicator of fluid saturation and lithology for rocks and soils. In the presence of fluid-filled pores (cracks, pores or open grain junctions), Vp/Vs will increase because Vs is relatively insensitive to pore filling materials (Mavko et al., 2020). Additionally, Vs<760 m/s is generally considered soil and not rock (Building Seismic Safety Council (BSSC) 2009) and fluid filled soils and rocks have Vp>1500 m/s. Thus, we compute Vp, Vs and Vp/Vs for Line 7 to differentiate soils from rock and saturated from dry materials (Fig. 5).

Our Vp tomogram (Fig. 5) produced an RMS error of 2.6 ms, and shows Vp from slightly less than 1500 to about 3600 m/s. Besides the shallowest portions of the profile between 420 and 520 m distance, Vp measured above 1500 m/s. Thus, we interpret essentially no unsaturated sediments to lie beneath Line 7. Vp greater than 3000 m/s is consistent with unfractured saturated sandstone (Table 1), and we identify these velocities near the bottom of our Vp tomogram between 0 and 300 m distance and between 360 and 500 m distance. Between 290 to 350 m distance, we observe a ~60 m wide LVZ that extends to the base of our model. We note that slower first arrival travel times were observed on the shot records and COG profiles (Fig. 2), consistent with our modeled results. In this region, Vp measures between 2000 and 2500 m/s and is bound by the two mapped fault traces. The LVZ is coincident with the elevated CO_2 flux measurements (Jung et al., 2014), the Jmb mapped extent, and the location of the CO_2-charged artesian springs that were identified during our campaign. This zone is also is consistent with the width of the LVZ mapped beneath Line 2.

Our Vs model, with a higher RMS error of 6.9 ms, shows Vs that ranges from 500 to 1750 m/s (Fig. 5). Outside of the central portion of the profile, Vs ranges from 500 to 1800 m/s. Vs greater than 750 m/s is noted for most of the profile, and is consistent with weathered rock and not soil at shallow depths. Between 290 to 350 m distance, we observe a slow Vs, low gradient zone. We measure Vs<760 m/s within the upper 10 m, consistent with soil and not rock. Although Vs increases with depth, the velocity within this zone remain anomalously low when compared to other portions of the profile.

Along most of our profile, we measure Vs that is consistent with rock from the upper few meters to the bottom of our model. The transition from dry to saturated rock is difficult to assess, as Vp can overlap for high ϕ saturated rock and low ϕ dry rock (Table 1). Between 290 to 350 m distance, we interpret the LVZ to represent the LGWF damage zone. Within this zone, we observe Vp/Vs>3, consistent with saturated soils or regolith. The elevated CO_2 flux values and artesian spring identified at this location support our interpretation of upward flowing fluids within a broad damage zone.

Our Line 7 reflection profile shows little reflectivity to the north of the LGWF. This may be related to the low power sledgehammer source that we utilized or related to altered bedrock within the footwall block. In contrast, we observe near flat lying reflectors to the south of the LGWF. We attribute this reflection pattern to represent an unfaulted hanging wall block within Km shale. Reflector terminations are consistent with a 60° north-dipping normal fault.

Because we transition from dry to saturated rock, and from sandstones to mudstones across the LGWF, ϕ estimates are difficult to quantify for Line 7. However, regardless of the approach, we interpret the sediments that lie within the damage zone to represent a high ϕ and high permeability steeply dipping conduit.

We estimate fracture density for Line 7 (Fig. 6). Although we acknowledge the same uncertainties with materials that fill the pore space, we assume $V_f = 1500$ m/s for the Vp tomogram and $V_f = 500$ m/s for the Vs tomogram. Using V_r to represent the fastest measured velocity from each tomogram, we estimate a fracture density approaching 50% at shallow depths and within the LGWF damage zone. We mask all fracture density estimates for Vp greater than 2000 m/s and Vs greater than 760 m/s, but we acknowledge the transition from regolith to competent rock may be gradational (e.g. Lebedeva and Brantley, 2013). Regardless of the assumptions, we note low fracture density rock within the both the fault's footwall and hanging wall below about 20 m depth. The vertically averaged fracture density estimates from Vp and Vs datasets show consistent results, supporting our observation of a ~30% change in fracture density within the fault zone when compared to the adjacent

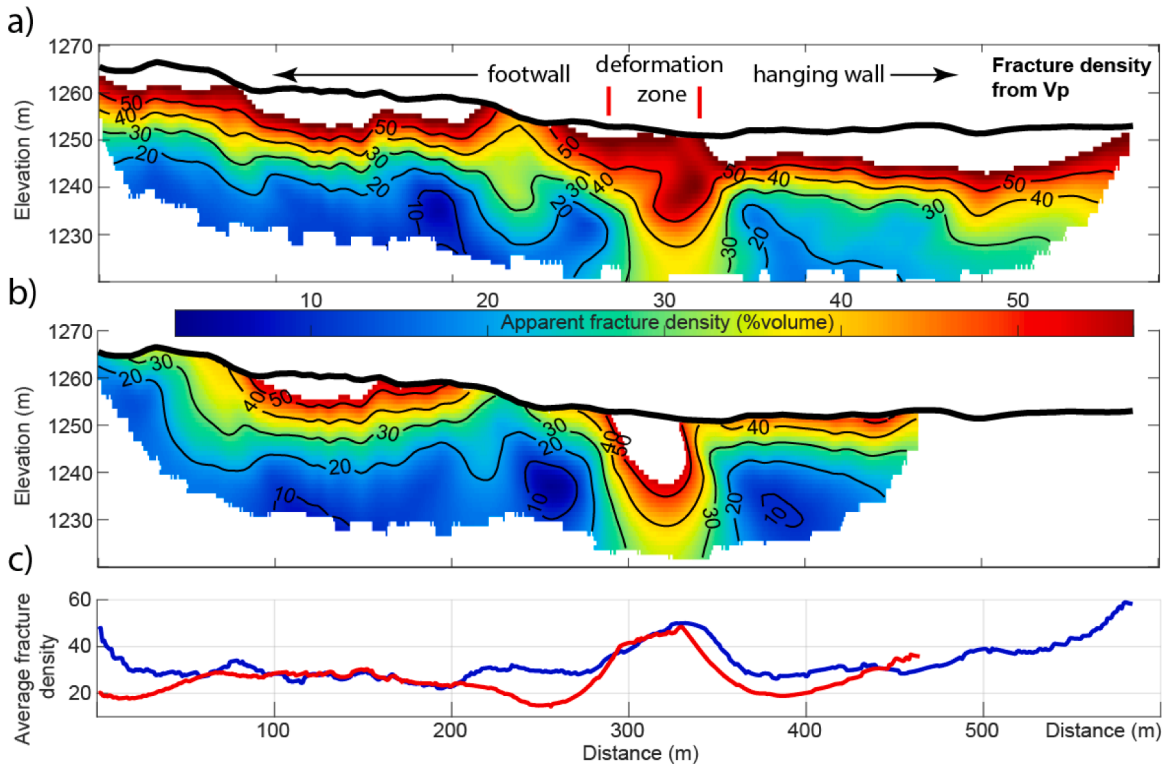

Fig. 6. Line 7 apparent fracture densities derived from: a) Vp tomogram using 1500 m/s for the pore-filling saturated sediments; b) Vs tomogram where we use 500 m/s for the pore-filling sediments; c) Vertically averaged fracture densities. Blue line represents Vp-derived (a) average fracture density and red line represents Vs-derived (b) average fracture density.

host rock. This exercise emphasizes that even below the regolith depth within the damage zone, we identify highly fractured bedrock.

In summary, Line 7 shows little evidence for sediment or regolith outside of the central LVZ damage zone that coincides with two strands of the LGWF. A change in fluid saturation and fracture density is noted outside of the damage zone, and fully saturated, highly fractured materials occupy the damage zone. Reflection results are consistent with one or two 60° south dipping normal faults and unfaulted hanging wall strata.

9. Discussion

Our seismic tomography data provides physical property estimates for the upper 20 to 40 m depth within a damage zone associated with the LGWF and for the adjacent host rock. We generate ϕ and fracture density estimates from our seismic velocities that we compare with CO_2 flux rates and to surface and river (groundwater) elevations. We use seismic reflection images to place the shallow velocities in a structural and stratigraphic context.

The observed 60 m wide LVZ on Lines 2 and 7 coincides with the main strand of the LGWF. Here, we observe a seismic velocity decrease, and fracture density increase of about 30% or more above the adjacent host rock. This damage zone width is greater than observed in outcrop. Although we acknowledge some uncertainties in velocity structure derived from our tomography approach, we note that Gettemy et al. (2004) directly related a 30% decrease in seismic velocity to a fault's damage zone at both laboratory and field scales; Isaacs et al. (2008) also showed similar and consistent results. Additionally, our measured damage zone width is globally consistent with fault systems of similar displacements (Savage and Brodsky, 2011; Torabi and Berg 2011; Schueller et al., 2013; Torabi et al., 2020). Here, we speculate that the increased ϕ within the fault zone relates to high fluid and gas pressure that has widened pre-existing microfractures (Naruk et al., 2019). For the upper 10 to 20 m, this process and expansion from decompaction linked to unroofing has converted host rock to soil either through mechanical processes, and/or through chemical dissolution (e.g., Lebedeva and Brantley, 2013).

Elevated CO_2 flux values and gas bubbles surfacing along Lines 2 and 7 reinforces our interpretation that the damage zone represents a high permeability vertical pathway. Here, CO_2 delivery to the critical zone and to the atmosphere is driven by advective flow through one or more vertical conduits. With the limited resolution of datasets available, the exact architecture of the fracture system that transport fluids cannot be constrained; however, migration along localized fracture corridors as outlined by Ogata et al. (2014) suggest fluid migration in narrower, tabular zones rather than large rock volumes. Similar scenarios are advocated by Caine et al. (1996) and Ganerød et al. (2008), with an emphasis on the inner part of the damage zone, near the fault core. With the observed change in seismic velocities for a 60 m wide zone, discrete seep-pipes or corridors are not detectable. Therefore, elevated fluid pressure in fractures of the footwall damage zone of the fault is likely causing the change in signal.

The different lithology and depositional age of the materials that occupy the fault zone for Lines 2 and 7 (Figs. 3 and 5) suggest that the damage zone is less sensitive to lithology of the surrounding host rock (Js and Jmb, respectively) and more sensitive to post-depositional processes and elevated pore pressures from the underlying reservoirs. The higher CO_2 soil flux values measured along Line 7 compared to Line 2 suggest that surface elevation is also not the primary driver for CO_2 delivery to the surface, as the damage zone along Line 7 is more than 20 m higher in elevation than that identified on Line 2, and one km farther in distance from the shallow groundwater adjacent to the Green River.

Modestly elevated CO_2 flux values were observed between fault strands of Line 2 (Fig. 3). Here, we relate slower Vp values near the bottom of our model to an increase in fracture density that was observed in the shallow portions of drillhole CO2W55. We note that the depth to the 1500 m/s contour, a proxy for water saturation, is elevated between 350 and 450 m distance on Line 2 when compared region farther north.

This may provide further evidence for elevated pore pressure within a broadly faulted or fractured zone; consistent with advective and not diffusive processes are driving CO_2 to the surface through bedrock fractures.

We identify two locations where we map faults without elevated CO_2 soil flux measurements. For example, at position 690 m distance of Line 2, we show seismic evidence for a fault (Fig. 3), consistent with outcrop patterns. Here, the depth to the 1500 m/s contour remains near river levels, and low permeability host or regolith may inhibit upward flow of CO_2 to the surface. We observe anomalously high velocities within the LGWF along Line 5 that is consistent with a low ϕ fault zone (Fig. 4). In outcrops, below remains of surface travertine, this fault zone hosts bed-subparallel to bed-normal carbonate veins in a stockwork, in concert with extensive carbonate cement filling initially porous rocks. These observations support a two-scenario (ongoing fluid migration versus sealed seeps), three-dimensional understanding of the permeability distribution, and hence insight into geophysical signals anticipated from former and current fluid migration paths in the near-surface. Both fluid migration along faults and near-surface CO_2 signatures are critical insight for any proposed CCS project.

10. Conclusion

This study explores the signatures of fluid migration out of porous containments into breached sealing units, and to the surface. We link seismic properties to outcrop and CO_2 soil flux measurements, identifying signatures of both active and former, sealed fluid leakage pathways. Through our measurements, we characterize high permeability CO_2/fluid pathways and a sealed zone where mineral precipitation has presumably produced carbonate veins and reduced the upward CO_2 flow.

Seismic velocities can be used to estimate lithology, the presence of fluids, porosity (ϕ), and fracture density. We show low velocity zones that relate to high permeability, high CO_2 soil flux regions. The shallow damage zone represents velocities that mimic soil properties, with fluid filled fractures that open by elevated pressure that reduces effective stress on the fault system, driving upward CO_2 migration. The region of elevated CO_2-flux exceeds the width of the identified fault damage zone from surface mapping, consistent with an expanded high porosity regolith above an outgassing fault. Conversely, disconnected fracture systems of the host rock do not carry fluids. Our conclusions are consistent with previous studies where fluid migration in fault zones is localized to the structurally complex damage zones that experience high fluid pressure. There, out- of-containment fluid migration depends on the total fluid pressure rather than fluids or rock composition.

For the successful long-term storage of CO_2 where fluid pressures are applied at depth, it is essential to determine soil and underlying rock properties, especially the presence of steep fractures. Determining whether these fractures are fluid filled, and whether these fractures will regionally act as a conduit or barrier for fluid migration will greatly influence the viability of a storage system and hence any CCS project.

CRediT authorship contribution statement

Lee M. Liberty: Conceptualization, Methodology, Investigation, Supervision, Validation, Writing – original draft, Writing – review & editing. **Jonathan Yelton:** Investigation, Data curation, Formal analysis, Writing – original draft. **Elin Skurtveit:** Validation, Writing – review & editing. **Alvar Braathen:** Writing – review & editing, Funding acquisition. **Ivar Midtkandal:** Writing – review & editing, Funding acquisition. **James P. Evans:** Conceptualization, Writing – review & editing.

Declaration of Competing Interest

The authors declare that they have no known competing financial interests or personal relationships that could have appeared to influence the work reported in this paper.

Data availability

I have provided a link to all data presented in this manuscript in the Acknowledgement section

Acknowledgement

Funding for the research was awarded from the Research Council of Norway (RCN) through the COTEC project (RCN# 295061). Additional field support provided by Thomas Otheim and Steven Slivicki. Helpful manuscript comments from James St. Clair improved this manuscript. Data from this study is available at https://doi.org/10.7914/SN/4S_2019 (Liberty, 2019).

References

Allis, R., Chidsey, T., Gwynn, W., Morgan, C., White, S., Adams, M., & Moore, J. (2001, May). Natural CO2 reservoirs on the Colorado Plateau and southern Rocky Mountains: Candidates for CO2 sequestration. In Proceedings of the First National Conference on Carbon Sequestration (pp. 14-17). US Department of Energy, National Energy Technology Laboratory Washington, DC.

Annunziatellis, A., Beaubien, S.E., Bigi, S., Ciotoli, G., Coltella, M., Lombardi, S., 2008. Gas migration along fault systems and through the vadose zone in the Latera caldera (central Italy): Implications for CO2 geological storage. Int. J. Greenhouse Gas Control 2 (3), 353–372.

Antonellini, M., Aydin, A., 1994. Effect of faulting on fluid flow in porous sandstones: petrophysical properties. AAPG Bull. 78 (3), 355–377.

Baer, J.L., Rigby, J.K., 1978. Geology of the Crystal Geyser and environmental implications of its effluent. Grand County, Utah: Utah Geology 5 (2), 125–130.

Baker, A.A., 1946. Geology of the Green River Desert–Cataract Canyon region, Emery, Wayne, and Garfield Counties, Utah: U.S. Geological Survey Bulletin 951, 500, 122 p., plate 1, scale 1:62.

Barton, C.A., Zoback, M.D., Moos, D., 1995. Fluid flow along potentially active faults in crystalline rock. Geology 23 (8), 683–686.

Bergfeld, D., Evans, W.C., Howle, J.F., Farrar, C.D., 2006. Carbon dioxide emissions from vegetation-kill zones around the resurgent dome of Long Valley caldera, eastern California, USA. J. Volcanol. Geotherm. Res. 152 (1–2), 140–156.

Brocher, T.M., 2005. Empirical relations between elastic wavespeeds and density in the Earth's crust. Bull. Seismol. Soc. Am. 95 (6), 2081–2092.

Building Seismic Safety Council (BSSC), 2009. NEHRP Recommended Seismic Provisions for New Buildings and Other Structures (FEMA P-750). Federal Emergency Management Agency, Washington, D.C.

Burnside, N.M., Shipton, Z.K., Dockrill, B., Ellam, R.M., 2013. Man-made versus natural CO2 leakage: A 400 k.y. History of an analogue for engineered geological storage of CO2. Geology 41 (4), 471–474. https://doi.org/10.1130/G33738.1.

Caine, J.S., Evans, J.P., Forster, C.B., 1996. Fault zone architecture and permeability structure. Geology 24 (11), 1025–1028. https://doi.org/10.1130/0091-7613(1996)0242.3.CO;2.

Castagna, J.P., Batzle, M.L., Eastwood, R.L., 1985. Relationships between compressional-wave and shear-wave velocities in clastic silicate rocks. Geophysics 50 (4), 571–581.

Clarke, B.A., Burbank, D.W., 2011. Quantifying bedrock-fracture patterns within the shallow subsurface: Implications for rock mass strength, bedrock landslides, and erodibility. J. Geophys. Res. 116 (4) https://doi.org/10.1029/2011JF001987.

Doelling, H.H., Kuehne, P.A., Willis, G.C., Ehler, J.B., 2015. Geologic map of the San Rafael Desert 30′x 60′quadrangle, Emery and Grand Counties, Utah. Utah Geological Survey Map M-180. Scale 1, 100000.

Dockrill, B., Shipton, Z.K., 2010. Structural controls on leakage from a natural CO2 geologic storage site: Central Utah, U.S.A. J. Struct. Geol. 32 (11), 1768–1782. https://doi.org/10.1016/j.jsg.2010.01.007.

Ehrenberg, S.N., Nadeau, P.H., 2005. Sandstone vs. carbonate petroleum reservoirs: A global perspective on porosity-depth and porosity-permeability relationships. AAPG Bull. 89 (4), 435–445.

Flinchum, B.A., Holbrook, W.S., Grana, D., Parsekian, A.D., Carr, B.J., Hayes, J.L., Jiao, J., 2018. Estimating the water holding capacity of the critical zone using near-surface geophysics. Hydrol. Processes 32 (22), 3308–3326.

Ganerød, G.V., Braathen, A., Willemoes-Wissing, B., 2008. Predictive permeability model of extensional faults in crystalline and metamorphic rocks; verification by pre-grouting in two sub-sea tunnels, Norway. J. Struct. Geol. 30 (8), 993–1004.

Gettemy, G.L., Tobin, H.J., Hole, J.A., Sayed, A.Y., 2004. Multi-scale compressional wave velocity structure of the San Gregorio Fault zone. Geophys. Res. Lett. 31 (6), 1–5. https://doi.org/10.1029/2003gl018826.

Gibson, J.R., Walsh, J.J., Watterson, J., 1989. Modelling of bed contours and cross-sections adjacent to planar normal faults. J. Struct. Geol. 11 (3), 317–328.

Gutierrez, M., Katsuki, D., Almrabat, A., 2012. Effects of CO 2 injection on the seismic velocity of sandstone saturated with saline water. Int. J. Geosci. 3 (05), 908.

Han, W.S., Lu, M., Mcpherson, B.J., Keating, E.H., Moore, J., Park, E., et al., 2013. Characteristics of CO2-driven cold-water geyser, Crystal Geyser in Utah: Experimental observation and mechanism analyses. Geofluids 13 (3), 283–297. https://doi.org/10.1111/gfl.12018.

Heath, J.E., Lachmar, T.E., Evans, J.P., Kolesar, P.T., Williams, A.P., McPherson, B.J., Sundquist, E.T., 2009. Hydrogeochemical characterization of leaking, carbon dioxide-charged fault zones in east-central Utah, with implications for geologic carbon storage. Carbon sequestration and its role in the global carbon cycle 183, 147–158.

Heath, J.E., Lachmar, T.E., Evans, J.P., Kolesar, P.T., Williams, A.P., 2009. Hydrogeochemical characterization of leaking, carbon dioxide-charged fault zones in east-central utah, with implications for geologic carbon storage. Geophysical Monograph Series 183, 147–158. https://doi.org/10.1029/2006GM000407.

Holbrook, W.S., Riebe, C.S., Elwaseif, M.L., Hayes, J., Basler-Reeder, K.L., Harry, D., W Hopmans, J., 2014. Geophysical constraints on deep weathering and water storage potential in the Southern Sierra Critical Zone Observatory. Earth Surf. Processes Landforms 39 (3), 366–380.

Hood, J.W., & Patterson, D.J. (1984). Bedrock aquifers in the northern San Rafael Swell area, Utah, with special emphasis on the Navajo Sandstone (No. 78). Utah Department of Natural Resources, Division of Water Rights.

Isaacs, A.J., Evans, J.P., Kolesar, P.T., Nohara, T., 2008. Composition, microstructures, and petrophysics of the Mozumi fault, Japan: In situ analyses of fault zone properties and structure in sedimentary rocks from shallow crustal levels. J. Geophys. Res. Solid Earth 113 (12), 1–17. https://doi.org/10.1029/2007JB005314.

Jung, N.H., Han, W.S., Watson, Z.T., Graham, J.P., Kim, K.Y., 2014. Fault-controlled CO2 leakage from natural reservoirs in the Colorado Plateau, East-Central Utah. Earth Planet. Sci. Lett. 403, 358–367. https://doi.org/10.1016/j.epsl.2014.07.012.

Kampman, N., Bickle, M.J., Maskell, A., Chapman, H.J., Evans, J.P., Purser, G., et al., 2014. Drilling and sampling a natural CO2 reservoir: Implications for fluid flow and CO2-fluid-rock reactions during CO2 migration through the overburden. Chem. Geol. 369, 51–82. https://doi.org/10.1016/j.chemgeo.2013.11.015.

Lebedeva, M.I., Brantley, S.L., 2013. Exploring geochemical controls on weathering and erosion of convex hillslopes: Beyond the empirical regolith production function. Earth Surf. Processes Landforms 38 (15), 1793–1807.

Lee, M.W. (2003). Velocity ratio and its application to predicting velocities. US Department of the Interior, US Geological Survey.

Lewicki, J.L., Brantley, S.L., 2000. CO2 degassing along the San Andreas fault, Parkfield, California. Geophys. Res. Lett. 27 (1), 5–8.

Liberty, L.M. (2019): Active seismic imaging of a leaky CO2 fault system. International Federation of Digital Seismograph Networks. Dataset/Seismic Network. https://doi.org/10.7914/SN/4S_2019.

Liberty, L.M., St Clair, J., McKean, A.P, 2021. A Broad, Distributed Active Fault Zone Lies beneath Salt Lake City, Utah. The Seismic Record 1 (1), 35–45.

Maček, I., Pfanz, H., Francetič, V., Batič, F., Vodnik, D., 2005. Root respiration response to high CO2 concentrations in plants from natural CO2 springs. Environ. Exp. Bot. 54 (1), 90–99.

Marion, D., Nur, A., Yin, H., Han, D.H., 1992. Compressional velocity and porosity in sand-clay mixtures. Geophysics 57 (4), 554–563.

Mavko, G., Mukerji, T., Dvorkin, J., 2020. The Rock Physics Handbook. Cambridge University press.

Miocic, J.M., Gilfillan, S.M.V., Frank, N., Schroeder-Ritzrau, A., Burnside, N.M., Haszeldine, R.S., 2019. 420,000 Year Assessment of Fault Leakage Rates Shows Geological Carbon Storage Is Secure. Sci. Rep. 9 (1), 1–9. https://doi.org/10.1038/s41598-018-36974-0.

Michael, A.J., Eberhart-Phillips, D., 1991. Relations among fault behavior, subsurface geology, and three-dimensional velocity models. Science 253 (5020), 651–654.

Moser, T.J., 1991. Shortest path calculation of seismic rays. Geophysics 56 (1), 59–67.

Naruk, S.J., Solum, J.G., Brandenburg, J.P., Origo, P., Wolf, D.E., 2019. Effective stress constraints on vertical flow in fault zones: Learnings from natural CO2 reservoirs. AAPG Bull. 103 (8), 1979–2008. https://doi.org/10.1306/12181817393.

Nur, A., Mavko, G., Dvorkin, J., Galmudi, D., 1998. Critical porosity: A key to relating physical properties to porosity in rocks. The Leading Edge 17 (3), 357–362.

Ogata, K., Senger, K., Braathen, A., Tveranger, J., 2014. Fracture corridors as seal-bypass systems in siliciclastic reservoir-cap rock successions: Field-based insights from the Jurassic Entrada Formation (SE Utah, USA). J. Struct. Geol. 66, 162–187. https://doi.org/10.1016/j.jsg.2014.05.005.

Pacala, S., Socolow, R., 2004. Stabilization wedges: solving the climate problem for the next 50 years with current technologies. Science 305 (5686), 968–972.

Patil, R.H., 2012. Impacts of carbon dioxide gas leaks from geological storage sites on soil ecology and above-ground vegetation. Divers. Ecosyst. 2, 27–50.

Prasad, M., Zimmer, M.A., Berge, P.A., & Bonner, B.P. (2004). Laboratory measurements of velocity and attenuation in sediments. LLNL Rep. UCRL-JRNL, 205155, 34.

Probst, A.J., Ladd, B., Jarett, J.K., Geller-Mcgrath, D.E., Sieber, C.M.K., Emerson, J.B., et al., 2018. Differential depth distribution of microbial function and putative symbionts through sediment-hosted aquifers in the deep terrestrial subsurface. Nat. Microbiol. 3 (3), 328–336. https://doi.org/10.1038/s41564-017-0098-y.

Rahman, F.A., Aziz, M.M.A., Saidur, R., Bakar, W.A.W.A., Hainin, M.R., Putrajaya, R., Hassan, N.A., 2017. Pollution to solution: Capture and sequestration of carbon dioxide (CO2) and its utilization as a renewable energy source for a sustainable future. Renewable Sustainable Energy Rev. 71, 112–126.

Ridgley, J.L., & Hatch, J.R. (2013). Geology and oil and gas assessment of the Todilto Total Petroleum System, San Juan Basin Province, New Mexico and Colorado: Chapter 3 in Total petroleum systems and geologic assessment of undiscovered oil and gas resources in the San Juan Basin Province, exclusive of Paleozoic rocks, New Mexico and Colorado (No. 69-F-3). US Geological Survey.

Savage, H.M., Brodsky, E.E., 2011. Collateral damage: Evolution with displacement of fracture distribution and secondary fault strands in fault damage zones. J. Geophys. Res. Solid Earth 116 (3). https://doi.org/10.1029/2010JB007665.

Schueller, S., Braathen, A., Fossen, H., Tveranger, J., 2013. Spatial distribution of deformation bands in damage zones of extensional faults in porous sandstones: Statistical analysis of field data. J. Struct. Geol. 52, 148–162.

Schuster, G.T., Li, J., Lu, K., Metwally, A., AlTheyab, A., Hanafy, S., 2017. Opportunities and pitfalls in surface-wave interpretation. Interpretation 5 (1), T131–T141.

Shipton, Z.K., Evans, J.P., Kirchner, D., Kolesar, P.T., Williams, A.P., & Heath, J. (2004). Analysis of CO2 leakage through "low-permeability" faults from natural reservoirs in the Colorado Plateau, southern Utah. In: Baines, S.J. & Worden, R.H. (eds.). Geological Storage of Carbon Dioxide. Geological Society, London, Special Publications 233, 43–58.

Skurtveit, E., Sundal, A., Bjørnarå, T.I., Soldal, M., Sauvin, G., Zuchuat, V., et al., 2020. Experimental Investigation of Natural Fracture Stiffness and Flow Properties in a Faulted CO2 Bypass System (Utah, USA). J. Geophys. Res. Solid Earth 125 (7). https://doi.org/10.1029/2019JB018917.

Skurtveit, E., Torabi, A., Sundal, A., Braathen, A., 2021. The role of mechanical stratigraphy on CO2 migration along faults–examples from Entrada Sandstone, Humbug Flats, Utah, USA. Int. J. Greenhouse Gas Control 109, 103376.

Clair, J. (2015). Geophysical Investigations of Underplating At the Middle American Trench, Weathering in the Critical zone, and Snow Water Equivalent in Seasonal Snow. PhD dissertation, Univ. of Wyoming.

Stockton, S.L., & Balch, A.H. (1978). The utility of petroleum seismic exploration data in delineating structural features within salt anticlines (No. 78-591). US Geological Survey.

Todd, T., Simmons, G., 1972. Effect of pore pressure on the velocity of compressional waves in low-porosity rocks. J. Geophys. Res. 77 (20), 3731–3743.

Torabi, A., Berg, S.S., 2011. Scaling of fault attributes: A review. Mar. Pet. Geol. 28 (8), 1444–1460.

Torabi, A., Ellingsen, T.S.S., Johannessen, M.U., Alaei, B., Rotevatn, A., Chiarella, D, 2020. Fault zone architecture and its scaling laws: where does the damage zone start and stop?. Geological Society, London. Special Publications 496 (1), 99–124.

Uyanık, O., 2019. Estimation of the porosity of clay soils using seismic P-and S-wave velocities. J. Appl. Geophys. 170, 103832 https://doi.org/10.1016/j.jappgeo.2019.103832.

Vrolijk, P., Myers, R., Sweet, M.L., Shipton, Z.K., Dockrill, B., Evans, J.P., et al., 2005. Anatomy of reservoir-scale normal faults in central Utah: Stratigraphic controls and implications for fault zone evolution and fluid flow. GSA Field Guides 6 (13), 261–282. https://doi.org/10.1130/2005.fld006(13.

Yamabe, H., Tsuji, T., Liang, Y., Matsuoka, T., 2016. Influence of fluid displacement patterns on seismic velocity during supercritical CO2 injection: Simulation study for evaluation of the relationship between seismic velocity and CO2 saturation. Int. J. Greenhouse Gas Control 46, 197–204. https://doi.org/10.1016/j.ijggc.2016.01.011.

Yelton, J., 2021. Seismic Imaging of Active and Ancient CO 2 Pathways in the Little Grand Wash Fault. Doctoral dissertation, Boise State University.

Yilmaz, Ö., Tanir, I., Gregory, C., 2001. A unified 3-D seismic workflow. Geophysics 66 (6), 1699–1713. https://doi.org/10.1108/17410380410555871.

Zimmer, M.A., Prasad, M., Mavko, G., Nur, A., 2007. Seismic velocities of unconsolidated sands: Part 1—Pressure trends from 0.1 to 20 MPa. Geophysics 72 (1), E1–E13.

Zoback, M.D., Zoback, M.L., Mount, V.S., Suppe, J., Eaton, J.P., Healy, J.H., Wentworth, C., 1987. New evidence on the state of stress of the San Andreas fault system. Science 238 (4830), 1105–1111.